Soft Matter

Structure and dynamics of a two-dimensional colloid of liquid droplets

Journal:	*Soft Matter*
Manuscript ID	SM-ART-07-2019-001433.R3
Article Type:	Paper
Date Submitted by the Author:	26-Sep-2019
Complete List of Authors:	Klopp, Christoph; Otto von Guericke University, Institute of Physics Trittel, Torsten; Otto von Guericke Universitat Magdeburg Eremin, Alexey; Otto-von-Guericke University Magdeburg, Institute of Physics Harth, Kirsten; Otto-von-Guericke University Magdeburg, Institute of Physics Stannarius, Ralf; Otto von Guericke University, Institute of Physics Park, Cheol; University of Colorado at Boulder Maclennan, Joseph; University of Colorado, Physics and Liquid Crystal Materials Research Center Clark, Noel; University of Colorado, Department of Physics and FLCMRC

Journal Name

ARTICLE TYPE

Cite this: DOI: 10.1039/xxxxxxxxxx

Structure and dynamics of a two-dimensional colloid of liquid droplets

Christoph Klopp,*[a] Torsten Trittel,[a] Alexey Eremin,[a] Kirsten Harth,[a] Ralf Stannarius,†[a] Cheol S. Park,[b] Joseph E. Maclennan,[b] Noel A. Clark,[b]

Received Date
Accepted Date

DOI: 10.1039/xxxxxxxxxx

www.rsc.org/journalname

Droplet arrays in thin, freely suspended liquid-crystalline smectic A films can form two-dimensional (2D) colloids. The droplets interact repulsively, arranging locally in a more or less hexagonal arrangement with only short-range spatial and orientational correlations and local lattice cell parameters that depend on droplet size. In contrast to quasi-2D colloids described earlier, there is no 3D bulk liquid subphase that affects the hydrodynamics. Although the films are surrounded by air, the droplet dynamics are genuinely 2D, the mobility of each droplet in its six-neighbor cage being determined by the ratio of cage and droplet sizes, rather than by the droplet size as in quasi-2D colloids. These experimental observations are described well by Saffman's model of a diffusing particle in a finite 2D membrane. The experiments were performed in microgravity, on the International Space Station.

1 Introduction

The spontaneous self-organization of colloids has been widely studied[1,2]: attractive or repulsive interactions of colloidal particles lead to their assembly in clusters or regular lattices which often have unique optical, magneto-mechanical or electro-mechanical properties. Colloidal particles allow the study of the self-organization, crystallization and dynamics of mutually interacting particles and may be considered as 'mesoscopic atoms'. Such colloidal systems have been investigated in both three and two dimensions. Classical examples are studies of structure formation[3,4], of the dynamics of the colloidal particles[5–8], of glass transitions, and of crystallization and melting[9–20].

Most of the 2D studies deal with solid, spherical particles trapped at horizontal air-liquid interfaces or at the interface between two fluids, or sedimented at the bottom of a fluid-filled container[21]. Even though the arrangement of colloidal particles in these systems is structurally two-dimensional, the dynamics are significantly distinct from those of a truly 2D system. All flow processes involve the 3D subphase and thus the flow field associated with the lattice dynamics is essentially that of a three-dimensional system. In some experiments, the particles are confined to a single layer in a thin cell (e. g.[10,18]). In this geometry, however, the cell boundaries influence the dynamics and phase behaviour of the particles in the layer[14]. Confinement to two dimensions can also be achieved by suspending solid particles in thin, fluid, free-standing films[22] but in such films it is difficult to avoid drainage and to keep the film thickness constant.

Here we introduce a system that resembles a colloid with genuine 2D dynamics: droplets in freely suspended smectic A (SmA) liquid-crystalline films. The structural properties of these assemblies are comparable to those of the above-mentioned quasi-2D systems. The dynamics, however, are distinctly different from 3D and quasi-2D colloids as will be shown here experimentally and by numerical modeling. The hydrodynamic interactions between

[a] Institute of Physics, Otto von Guericke University, D-39106 Magdeburg, Universitätsplatz 2, Germany.
[b] Soft Materials Research Center, Physics Department, University of Colorado, Boulder, CO 80309, USA
∗ christoph.klopp@ovgu.de, † ralf.stannarius@ovgu.de

the droplets are mediated only by the thin film in which they are suspended, and any diffusion of the droplets and reorganization of the lattice is constrained by hydrodynamic processes in that 2D fluid.

The smectic A phase (SmA) consists of elongated mesogens that arrange in layers, where the mean orientation of the molecular long axes (optical axis) is normal to the layer planes, and the phase symmetry is $T(2) \times D_{\infty h}$. The material can form stable thin, freely suspended films in air. The dynamics of single inclusions in such films have been described previously[23–25]. A transition from 3D to 2D dynamics was observed by varying the thicknesses and lateral dimensions of the film. While earlier studies dealt with single inclusions or isolated pairs of inclusions, we consider here the self-organization of ensembles of many inclusions into colloidal lattices. We have analyzed the structure and dynamics of these arrangements.

In smectic C films, self-organization of droplets has been described previously[26–32]. Smectic C films are anisotropic in the film plane, and spatial variations of the local tilt azimuth, described by the c-director, can mediate attractive or repulsive interactions between inclusions in such films. In contrast, the SmA films studied here are isotropic in the film plane. Since there is no molecular tilt, there are no elastic interactions between the inclusions. Locally, the films supporting the inclusions are uniformly thick on a molecular scale so that we can also neglect any capillary interactions between droplets.

2 Experimental setup and materials

Smectic bubbles with centimeter diameters are prepared by a technique introduced in Refs.[33,34] using an automatic setup described in detail in Ref.[35]: A flat, free-standing film initially spanning the opening of a metal syringe is inflated with air so that it becomes spherical. Figure 1a shows the top of the inflation syringe with the smectic bubble sessile on it. The experimental setup contains additional elements such as the airjet needles seen at the top of the image, which are not relevant to the present experiment. In principle, the film thickness can be kept constant when the bubble is inflated sufficiently slowly. Additional smectic material for the expanding bubble is delivered continuously from the meniscus around the syringe. Inhomogeneously thick bubbles such as seen in Fig. 1 can occur for several reasons, for example when the inflation speed is not kept constant. Then, the film contains large, uniform regions separated by discrete thickness steps, a well-known feature of freely suspended smectic films. These inhomogeneities disappear after some annealing time, which in the present system may be of the order of several minutes up to hours. The film curvature can be neglected at the scale of the droplet lattices.

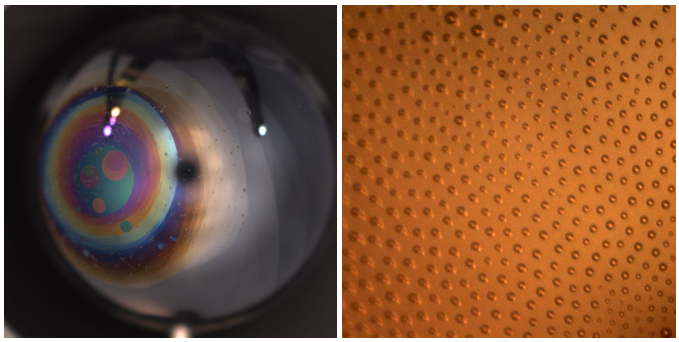

a) b)

Fig. 1 a) Macroview of a smectic bubble 15 mm in diameter on the ISS, viewed in reflected light. The capillary for inflation is visible at the bottom. The top of the bubble is obscured in the image by needles used for blowing air across the film[35]. Colors reflect local background film thicknesses, with discrete layer steps. Droplets are not resolved at this magnification. b) Microview of a $500 \times 500\ \mu\text{m}^2$ region of the bubble surface, showing a uniformly thick background film and a typical droplet lattice. A video in the supplemental material shows an example of the lattice dynamics in real time.

The inclusions, which are microdroplets of the same material as the supporting film, form when the film is heated sufficiently rapidly to a temperature slightly above the bulk transition to the isotropic or nematic phase[27,36]. Under these conditions, some of the inner layers of the film melt and the molten material forms droplets as seen in Fig. 1b, in a spinodal separation process. Because the surface tension of the droplets is slightly larger than that of the smectic film, these droplets adopt the shape of very flat lenses[36]. Their radii R are of the order of few micrometers to a few dozen micrometers, and they have aspect ratios (droplet thickness to droplet diameter) between 0.13 and 0.17, depending upon temperature.

The molten droplets remain in coexistence with the SmA background film. With a suitable heating protocol, one obtains locally rather uniform droplet sizes. Over longer distances (several mm), droplet sizes vary because the heating rate during droplet creation is not uniform everywhere on the bubble surface. After preparation, these droplets can be kept stable for hours under isothermal conditions. In order to avoid gravitational sedimentation of the droplets, and to prevent buoyancy-driven convection of the air surrounding the film, the experiments were performed in microgravity ($< 10^{-3} g$) on the International Space Station (ISS). Under normal gravity, similar experiments could only be performed us-

ing flat, horizontal films. In this case, the meniscus around the film and its interactions with inclusions in the film cannot be ignored. In the bubble geometry, on the other hand, the meniscus at the syringe is very small and its influence on the film is negligible.

A remarkable feature of the droplets that has not been described previously in SmA films is that they spontaneously form extended lattices with short-range order. The cells of the lattice are not very regular, as is evident from Fig. 1b. This lattice has appreciable dynamics, with the individual cells continuously reorganizing, and the lattice moving together with the surrounding film material on the bubble surface. The macroview in Fig. 1a shows that the film thickness is not uniform across the bubble, but there are large regions of uniform film thickness. The boundaries of these regions form natural borders that confine the droplets[36], so that the droplet arrays are trapped within the uniformly thick regions. In clusters of a few hundred or thousand droplets, they are rather monodisperse, but in general the droplet and lattice sizes vary in different parts of the bubble surface.

The experimental setup includes two cameras, which provide complementary views: a macroscopic view of the entire bubble, and a small magnified region of the bubble surface as shown in Fig. 1a,b. The magnified region is located a few millimeters right of the top of the bubble shown in the macroview. The maximum frame rate of the cameras is 30 fps. Droplet positions are extracted from the recorded images using tracking software that provides the positions and diameters of the droplets with an accuracy of ≈ 0.5 μm. The liquid crystal material investigated is a commercial mixture (Displaytech MX 12160), with phase sequence Isotropic 51.1°C SmA -3.2°C Cryst (3.1°C SmA).

3 Observations and data analysis

3.1 Lattice structure

First we analyze the structure of the droplet arrangements. The lattice is stabilized by repulsive interactions between the droplets. Elasto-capillary interaction forces have been described for spherical inclusions in smectic films[37]. However, the droplets observed here are too flat to have detectable menisci. The embedding film is uniformly thick so that long-range capillary forces can be excluded. In addition, because SmA films are isotropic in the plane of the film and there is no molecular tilt, any elastic interactions between the inclusions mediated by orientational elasticity of the film are negligible.

The nature of the repulsive interactions between the droplets is not fully understood. The main contribution to the repulsive forces is presumably electrostatic. The droplets are slightly negatively charged. This can be demonstrated by placing an electrode needle at a high potential ($\approx$ 150 V relative to the film holder) close to the film. When the needle potential is positive, droplets move along the film, towards the needle. When the electric potential of the needle is reversed, the droplets are repelled. Similar electrostatic effects have been reported earlier[34] in smectic islands on bubbles exposed to large electric fields. One of the reasons for the charging of the droplets may be an overall electric charge of the bubble after inflation, and an accumulation of charges in islands or droplets. It may also be that ions present in the LC material, particularly bulky anions, have a tendency to accumulate in isotropic material, being expelled by the ordered smectic phase of the film. Such electrostatic interactions will be partially screened by ions in the background film. However, since the film thickness (about a dozen molecular layers, i. e. a few dozen nanometers) is much smaller than the droplet height, screening is incomplete. The density of counter-ions in the thin film is not sufficient to fully screen the electrostatic interactions and the Debye length is of the order of dozens or maybe hundreds of micrometers.

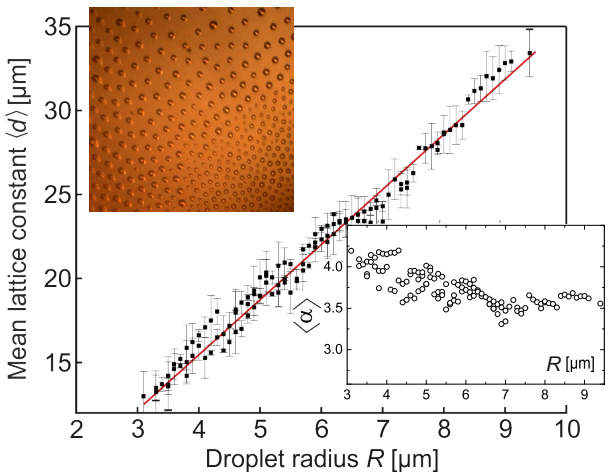

Fig. 2 Lattice geometry: mean lattice constant $\langle d \rangle$ (mean distance to the centers of the neighboring droplets) vs. droplet radius R. The variation is essentially linear, with $\langle d \rangle = 3.25R + 2.5$ μm. The solid red line is a linear fit. The upper inset shows a typical 500×500 μm^2 image of coexisting regions with different droplet and unit cell sizes. The lower inset shows the dependence of the average cell aspect ratio $\langle \alpha(R) \rangle = \langle d \rangle / R$ on droplet size.

The droplets form a local lattice with predominantly hexagonal cells, tending to maximize the distances between nearest neighbors. The film area over which a droplet array can spread is bounded by dislocations (thickness steps of the films). Such thickness steps demarcate regions of uniformly thick background

film (identified by different colors in Fig. 1a) and form natural boundaries that the droplets cannot cross[36]. This geometrical confinement stabilizes the droplet arrays, which would otherwise tend to expand without bound.

When one constructs Voronoi cells with the droplets as generators (Wigner-Seitz cells), a quantitative analysis of snapshots (such as in Fig. 1b) shows that approximately 57 % of the cells are hexagons, 31 % are pentagons, 10 % are heptagons, and 2 % are tetragons. The lattice as a whole drifts with its confining domain in the film plane, with the local structure remaining essentially unchanged, but without long-range correlations. In the following, we perform model computations with the simplifying assumption that all of the cells are regular hexagons. One may carry out the same computations with a more realistic distribution of cell shapes, but then one has to sacrifice simplicity and the opportunity to employ analytical approaches to describe the potentials and the particle mobilities.

The ratio $\langle d\rangle/R$ between the mean lattice constant $\langle d\rangle$ (average distance to nearest neighbors) of unit cells containing droplets of radius R in one and the same film increases monotonically with R. For a first statistical characterization of the lattice properties, we average over cells with similar particle sizes to obtain the mean lattice constant as a function of the radius of the central particle. The result is shown in Fig. 2. The mean 'aspect ratio' $\langle\alpha\rangle \equiv \langle d\rangle/R$ of the unit cells, shown in the inset, is weakly dependent on R, with small droplets preferentially forming cells of slightly larger aspect ratios. For individual sites, $\alpha(R)$ ranges between 2.5 and 6. This will be important when we analyze the statistics of the droplet dynamics.

We now consider the total electrostatic potential $\phi(r)$ produced by the six nearest neighbors (all at the same radius) of a droplet at position P, expanding the potential to second order in the radial distance r of P from the center of the hexagon. We assume, to a first approximation, that there is a point charge q at the centre of each droplet, and we neglect Debye screening by ions in the thin background film. The potential due to each neighboring charge as a function of its distance r' from the point P is $\phi_1(r') = q/(4\pi\varepsilon_0 r')$. The net potential experienced by the central droplet (expanded to second order in r) is axially symmetric

$$\phi(r) \approx \frac{q}{4\pi\varepsilon_0 d}\left[6 + \frac{3r^2}{2d^2} + \mathscr{O}\left(\frac{r^4}{d^4}\right)\right]. \qquad (1)$$

Correction terms with sixfold symmetry enter only in fourth and higher orders of (r/d) and are ignored here. Equation (1) considers only the nearest neighbors, neglecting any charges further away, and may thus underestimate the steepness of the potential. Contributions from other sites separated by a distance d' from the origin decay as $1/d'^3$, and lead to a finite correction factor in the r^2 term of Eq. (1), deepening the potential. In order to estimate the magnitude of such a correction, we computed the potential near the origin for an infinitely extended perfect triangular lattice (Appendix A). For such a perfect lattice, the correction factor would be 1.836. Note, however, that these additional interactions are largely averaged out for two reasons: First, long-range electrical interactions are screened by counterions in the film, which acts as a weak electrolyte. More importantly, the aforementioned fluctuations of the lattice reduce the influences of charges beyond the next neighbors. The actual forces in our experiments may therefore be somewhat larger than those predicted by Eq. (1), but the general form of the potential is adequate and the calculated forces are of the right order of magnitude.

In the approximation of Eq. (1), a central particle with charge q experiences a radial force $F = -d(q\phi)/dr$:

$$F = -Kr \approx -\frac{3q^2}{4\pi\varepsilon_0 d^3} r \qquad (2)$$

and the particle distribution in the cage is expected, on average, to be axially symmetric. The force constant K can be extracted from the spatial distribution of the central droplet positions. The distribution

$$\rho(r) = \rho_0 r \exp\left(-\frac{Kr^2}{2k_B T}\right), \qquad (3)$$

assuming a Boltzmann distribution in 2D with axial symmetry, has its maximum at $r_{\max} = \sqrt{k_B T/K}$. An analysis of the spatial excursions of droplets of a given size yields the distribution shown in Fig. 3a. From the maximum of this distribution, one obtains a force constant $K \approx 0.3$ nN/m. While small fluctuations from the center (< 7 μm) are well represented by Eq. (3), the observed large fluctuation tail clearly deviates from that prediction. The main reason is that the cages are not perfectly hexagonal, so that larger excursions occur more frequently than expected. We note that this calculation is a rough approximation since we have no quantitative information of the screening effects. If the Debye length is of the order of d, then the potential generated by the six outer droplets will be partially screened, and thus larger droplet charges q may have to be assumed. If the Debye length actually is much larger than d, one may have to include more neighbors in the calculation of the potential in the cell. In any case, the functional form of the potential in the center of the cage will not change to leading order.

The assumption of point charges is a convenient but crude approximation. A more reasonable assumption is that the charges

are either distributed uniformly over the droplet area, approximated by a uniformly charged disk with radius R, or, even more realistically, that the charges of the same sign within each droplet repel each other, and thus are confined to the droplet circumference, still remaining in the isotropic region. Such arrangements lead to quadrupolar corrections to $\phi_1(r')$ in the film plane, of the form $\phi_1(r') = q/(4\pi\varepsilon_0 r') \cdot [1 + \xi R^2/r'^2]$ with $\xi = 1/4$ for the ring and $\xi = 1/8$ for the disk. The correction terms are obtained by expanding the well-known potentials of homogeneously charged rings or disks. These higher order corrections do not affect the second order term in Eq. (1), they enter this equation only in $\mathcal{O}(r^4/d^4)$. However, they would both lead to a suppression of the tail of the theoretical distribution in Fig. 3a for large r, increasing the mismatch with the experiment.

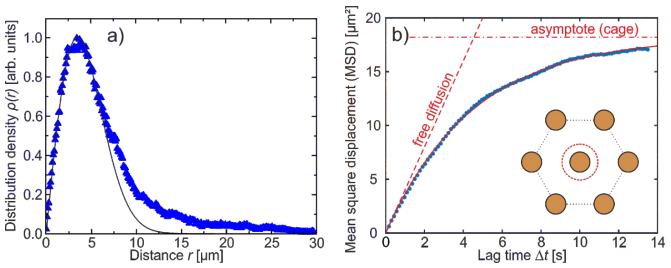

Fig. 3 a) Distribution density $\rho(r)$ of the positions of the central droplets with radius $R = 4.05 \pm 0.25$ μm in the cage, averaged over all droplets of this size. The solid line is a fit of the small r data ($r < 7$ μm) using Eq. (3). The systematic deviations for large fluctuations may result from asymmetries of the cages and a non-harmonic potential. b) Typical time dependence of the mean square displacement from the center of the cage (Eq. (4)), averaged over all droplets in the radius range $R = 5.66 \pm 0.25$ μm and cell aspect ratio range 4.75 ± 0.21. The inset sketches the central particle with the neighbors forming the cage. The dashed circle is the approximate region in which the particle position fluctuates.

3.2 Droplet dynamics

In order to analyze the individual droplet dynamics, we subtract the local drift of the lattice and evaluate the droplet diffusion relative to the cage formed by the six nearest neighbors (the mean square displacement, MSD, relative to the cage). A typical MSD curve, obtained by analyzing 500 images with 400 ± 20 droplets each, is shown in Fig. 3b. The solid line is a fit assuming diffusion in a parabolic potential,

$$\mathrm{MSD} \equiv \langle \Delta r^2(\Delta t) \rangle = \frac{4k_BT}{K}\left[1 - \exp\left(\frac{-KD\Delta t}{k_BT},\right)\right] \qquad (4)$$

where D is the 'free diffusion' coefficient of the central droplet. The asymptotic value of $\langle \Delta r^2(\Delta t) \rangle$ for large Δt yields $4k_BT/K$, providing another means of determining the force constant K. Since the system is ergodic, K obtained this way agrees with that from the stationary distribution density (Fig. 3a). The dashed circle in the inset of Fig. 3b has a radius equal to the square root of the asymptotic MSD $\lim_{\Delta t \to \infty} \langle \Delta r^2(\Delta t) \rangle$, marking the approximate extent of the zone in which the central particle diffuses.

Figure 4 shows the force constants determined for droplets with different cell aspect ratios from the asymptote of the MSD. Figure 4a contains the raw data of 5000 individual sites. In Fig. 4b, we have averaged data in bins of $\delta\alpha = 0.1$ width, to obtain mean values of the interaction force as a function of the cell aspect ratio. The force constant clearly increases for smaller aspect ratios. This is probably a reflection of the actual charge distribution (disk or ring like) in the droplets, which leads to larger effective force constants when the aspect ratio is smaller (the droplet boundaries are closer to each other). There is no obvious correlation of K with droplet radius R (graph not shown). An estimate of the net charges q necessary to produce the force constants shown in Fig. 4 yields $q \approx -10^{-17}$C, corresponding to only a few dozen negative excess elementary charges.

Whereas the long term, asymptotic value of the MSD provides information on the interaction potential, the short-time slope of the graph in Fig. 3b is determined by the particle mobility b alone. The term 'free diffusion' that we have chosen refers to the fact that the particle does not experience the influence of the potential during short intervals ($\Delta t \ll k_BT/(KD)$ in Eq. (4)). However, this mobility is significantly different from the diffusion of an individual free particle without neighbors, because the flow field generated by the droplet motion is 'disrupted' at the boundaries of the cage formed by the neighbors. This flow field is essentially confined to the quasi-2D film, the surrounding air playing only the role of a correction term.

Models for the mobility of single particles in 2D fluids have been developed primarily for the description of biological membranes[38–41]. In two dimensions, the mobility $b = v/F$ of a particle moving with velocity v under the action of a force F in a thin fluid film with thickness h and viscosity η, bounded by a second fluid with viscosity η', can be found from Saffman's equations[38,39], either considering the surrounding air (the 3D case), or lateral fixed boundaries of a circular film region (the 2D case). The Saffman length $\ell_S = \eta h/(2\eta')$ provides a criterion for deciding which of these two approximations applies. Thin films, where ℓ_S is shorter than their lateral dimensions, are more 3D like, whereas thicker films with ℓ_S exceeding the film width behave like 2D fluids. In

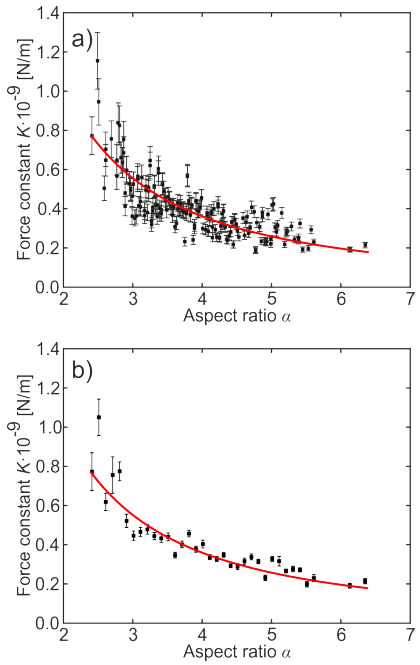

Fig. 4 Force constant $K(\alpha)$ determined from the asymptotic limit of the MSD (see Eq. (4)) vs. cell aspect ratio α. Measurements from 5000 individual unit cells are shown. The film thickness is 41 nm. (a) shows the complete set of data for all individual sites, (b) is obtained by averaging all cells with similar aspect ratios, with bin widths of $\delta\alpha = 0.1$. The solid red line is an empirical fit $K = 2.87\times10^{-9}\alpha^{-3/2}$ N/m, to guide the eye.

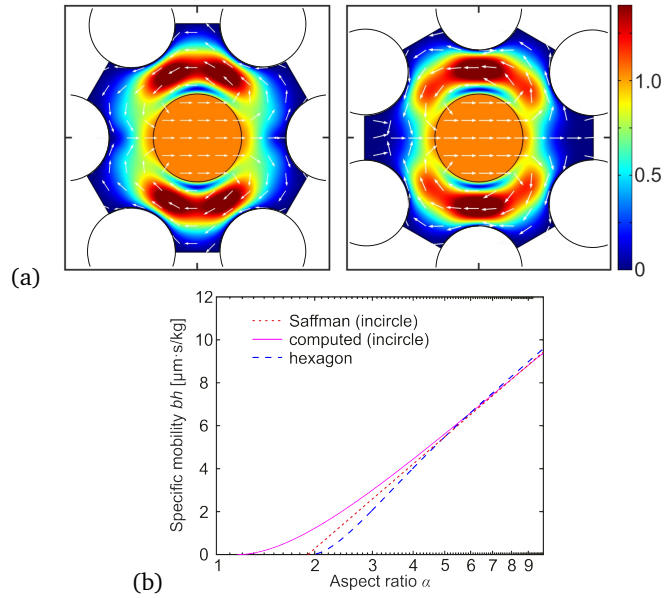

Fig. 5 (a) Flow fields around a moving particle in a cage formed by six neighbors of similar size, with $\alpha = 3.0$: (left) particle motion towards the nearest neighbor, and (right) towards the cell edge. The magnitude of the velocity is color-coded, in units of the central droplet velocity. Box sizes are $2d\times2d$. (b) Specific mobility $b' = bh$ as a function of the aspect ratio α for Saffman's model (dotted line), numerical result for a circular area with the incircle of the hexagonal cell (solid line) and exact numerical solution (dashed line).

our case, the experimentally determined viscosity of the mixture is $\eta = 14$ mPas. With h on the order of few dozen nanometers and η/η' on the order of 10^3, ℓ_S is between 10 and 100 μm, larger than the mean droplet separation. We may therefore ignore the air surrounding the film and consider the hydrodynamics of each caged droplet as being essentially 2D.

We computed the droplet mobility numerically for the case of a regular hexagonal lattice, using Finite Elements Methods (FEM) software (*COMSOL*), assuming that the flow field around a moving droplet is zero at the circumferences of the six neighbors and at the sides of the hexagonal unit cell. We set the velocity at the boundary of the central droplet to a constant value, solved the flow field numerically, and computed the net viscous force acting on the droplet by integrating the viscous stress at the droplet boundary. For a unit cell formed by droplets of uniform size, the cell aspect ratio α is the only free parameter, the droplet sizes being irrelevant[39]. This situation is roughly analogous to a particle diffusing in a circular film with non-slip flow at the boundaries[23]. There, the mobility is determined by the ratio of the film and particle radii alone[39].

Fig. 5a shows the unit cell and the flow field caused by the motion of the central droplet towards one of the nearest neighbors (left) and a next-nearest neighbor (right). Within our numerical precision, the calculated resulting drag forces are equal in the two cases. Fig. 5b shows the calculated specific mobilities $b' = bh$ as a function of the aspect ratio α (dashed line). The dotted line shows, for comparison, the analytical result of Saffman's model for a circular film,

$$b = \frac{1}{4\pi\eta h}\left(\ln\frac{R_S}{R} - 0.5\right). \qquad (5)$$

As a suitable equivalent radius R_S, we have chosen that of the incircle to the hexagon ($R_S = \sqrt{3/4}\,d$). This approximation is valid only for large aspect ratios[39], but it nevertheless still yields reasonable results for smaller aspect ratios, like those found in our lattices. The solid line in Fig. 5b is the numerical result for diffusion in the center of a circular film with radius R_S. It agrees with Saffman's analytical solution of Eq. (5) for large α. Since it ne-

glects the effective reduction in cage dimension due to the finite size of the six surrounding droplets, however, it understandably deviates considerably from the hexagon simulations at small α.

As seen in Eq. (5), droplet mobility depends solely on the aspect ratio α. They are therefore only indirectly (via $\alpha(R)$, see Fig. 2) dependent on actual droplet sizes, in contrast to freely moving inclusions[23,24].

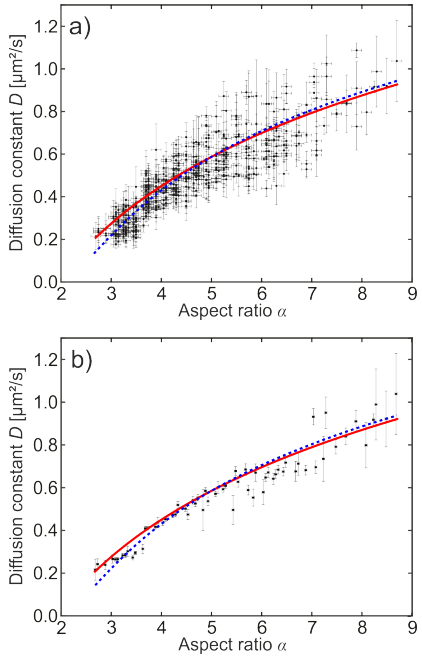

Fig. 6 Calculated diffusion coefficients $D = bk_BT$ vs. cell aspect ratio α and experimental data for individual droplets. The solid line is Saffman's solution, Eq. (5), for a circular boundary, while the dashed line shows the numerically computed curve for a hexagonal cell, see Fig. 5. (a) complete set of data for all individual sites, (b) is obtained by averaging all cells with similar aspect ratios, with bin sizes $\delta\alpha = 0.1$.

The diffusion coefficients $D = bk_BT$ determined using Eq. (4) are shown in Fig. 6. The dashed line shows the predictions of the numerical simulations using hexagonal cages, while the solid line is Saffman's approximation for a circular boundary with the radius of the inscribed circle of the hexagonal unit cells. As in the previous graphs for the force constant, we show one image with the complete data set (Fig. 6a) and the same data averaged over bins with widths $\delta\alpha = 0.1$ (Fig. 6b). Within experimental error, there is satisfactory agreement between the model and the experiment. The deviations from theory are mainly caused by variations in the shapes of the unit cells. Even though the majority of droplets have six neighbors, few of the cages are regular hexagons.

4 Summary

Lens-shaped droplets on SmA freely suspended films form a two-dimensional colloidal lattice with predominantly hexagonal unit cells because of mutually repulsive electrostatic interactions. The particle dynamics are distinctly different from those of 2D colloidal particles at fluid surfaces and interfaces. The droplet mobility depends solely on the ratio α of cage and droplet sizes. The observed diffusion behavior is described well by Saffman's model for the mobility of particles in a 2D fluid with restricting lateral boundaries.

An interesting option in this experimental system is that one could in principle tune the lattice constants and cell aspect ratios by inflating or deflating the bubble. For a given number of droplets, the lattice would be expected to expand or shrink with the smectic bubble radius. However, a prerequisite for such studies will be the availability of a microgravity environment such as provided by the ISS or suborbital rockets.

Acknowledgments

The Magdeburg group was supported by the German Aerospace Center (DLR) with project 50WM1744 and by the Deutsche Forschungsgemeinschaft (DFG) with project STA 425/40-1. C. K. acknowledges support by a Landesstipendium Sachsen-Anhalt.

The Colorado group was supported by NASA Grant NNX-13AQ81G and by the Soft Materials Research Center under NSF MRSEC Grant DMR-1420736.

Appendix A: Potential of the perfect triangular lattice

Equation (1) describes the potential of six electric point charges symmetrically arranged in a distance d around the origin. The strength of such a potential decreases with increasing d as d^{-3}. A crude estimate shows that the potential of an infinitely extended perfect triangular lattice in 2D will remain finite, in contrast to a 3D lattice. In 2D, the number of lattice points in distance d grows on average linearly with d, thus all charges in distance d contribute a term proportional to d^{-2} to the potential at the origin. The integral of these contributions over the complete lattice does not diverge but it remains finite. One can estimate an upper limit for this potential analytically, and calculate the exact value numerically.

For the exact mathematical treatment of the hypothetical perfect infinite lattice, we start with the solution for the potential created by six neighbors, Eq. (1). We subtract the constant term

and consider only only the lowest order contribution in r,

$$\tilde{\phi} = \phi(r) - \phi_0 = Q\frac{r^2}{d^3} \tag{6}$$

with the constants $Q = 3q/(8\pi\varepsilon_0)$ and $\phi_0 = 4Q/d$.

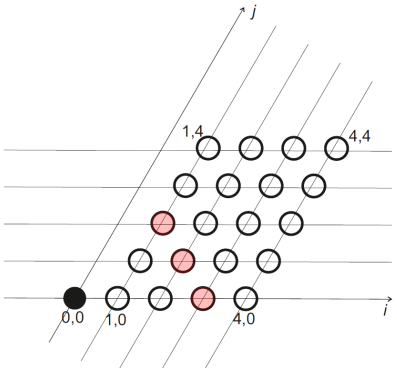

Fig. 7 Lattice geometry: the lattice sites are labeled by their coordinates i, j in one 60° sector around the central droplet, the other sectors are similar because of the sixfold symmetry axis. As an example of the definition of coordination regions (see text), sites belonging to $s = 3$ are filled light-red.

Now, we consider the additional contributions of all other droplets in the lattice. We introduce a non-orthogonal coordinate system i, j as shown in Fig. 7 and set the central droplet to the origin $(0,0)$. The other droplets with point charges q are at positions (i, j). The coordinates are given in units of the lattice constant d. We need to consider only a 60° sector as sketched in the figure, the other five sectors are similar for symmetry reasons. The six droplets in the nearest-neighbor model, Eq. (1), are the one at position $(1,0)$ and the corresponding sites in the remaining five sectors.

We define for convenience 'coordination regions' (in analogy to coordination spheres of crystals) by the number $s = i + j$ of unit steps along coordinates i and j that are necessary to reach a certain site starting from the origin. The distance of site (i, j) from the center is $d \cdot \sqrt{s^2 - ij}$. In coordination region s, all sites have distances from the origin between $d \cdot \sqrt{3/4}\, s$ and $d \cdot s$. Exactly s sites in the sector belong to each coordination region s: $(s,0)$, $(s-1,1),\ldots,(1,s-1)$. For instance, those of region 3 are filled light-red in Fig. 7. In order to compute the contribution ϕ_{ij} of site (i, j) and its equivalents in the remaining five sectors to the potential at the origin, one only needs to replace d in Eq. (1) by $d\sqrt{s^2 - ij}$. One finds

$$\phi_{ij} = \tilde{\phi}\,(s^2 - ij)^{-3/2} \tag{7}$$

One can calculate an upper and a lower estimate of the contribution ϕ_s of all sites in region s. Their distance to the origin is $\geq d \cdot \sqrt{3/4}\, s$, thus all s sites in that region together contribute

$$\phi_s < \phi_{s,\max} = s \cdot \tilde{\phi}\, s^{-3} \left(\frac{3}{4}\right)^{-3/2} \approx 1.54\,\tilde{\phi}\,\frac{1}{s^2} \tag{8}$$

We sum up all regions $s > 1$,excluding the nearest neighbors (1,0) that are already contained in Eq. (1). Exploiting

$$\sum_{k=1}^{\infty} \frac{1}{k^2} = \frac{\pi^2}{6} \approx 1.644,$$

we obtain

$$\phi_{\max} = \sum_{s=2}^{\infty} \phi_{s,\max} = 0.644 \cdot 1.54\,\tilde{\phi} \approx 0.993\,\tilde{\phi} \tag{9}$$

This finite value is an upper limit for the additional contributions to the potential of Eq. (1) for an infinitely extended lattice. We note in passing that a lower estimate is found when the maximum distance s of the charges in each region s is inserted, $\phi_{\min} = 0.644\,\tilde{\phi}$. The numerical computation of the exact factor is straightforward, it yields ≈ 0.8356. Probably, this result can even be obtained analytically. The conclusion is that the contributions of the outer sites in a perfectly ordered triangular lattice can be included in a finite correction factor of 1.8356 in Eq. (1), which makes the central potential steeper, but does not change the functional form. Of course, the constant term ϕ_0 subtracted in Eq. (6) increases with the number of lattice points so that the potential of an infinitely extended lattice would be infinite in the origin, but this is only an abstract mathematical feature without physical consequences. For any physical, arbitrarily large but finite lattice, this constant term remains finite and can be subtracted. For the actual forces acting on the central particle, it is irrelevant.

Finally, we emphasize again that the inclusion of far-reaching interactions requires a perfect long-range order which is clearly absent in our lattices, and no Debye screening. Thus we expect that Eq. (1) may somewhat underestimate the correct potential, but probably by no more than about 25 %.

References

1 P. N. Pusey and W. van Wengen, *Nature*, 1986, **320**, 340.
2 M. Grzelczak, J. Vermant, E. M. Fust and L. Liz-Marzán, *ACS Nano*, 2010, **4**, 3591.
3 F. J. Maier and T. M. Fischer, *Soft Matter*, 2016, **12**, 614.
4 V. Lotito and T. Zambelli, *Adv. Colloid Interface Sci.*, 2017, **246**, 217–274.

5 I. Williams, E. C. Oguz, P. Bartlett, H. Löwen and C. P. Royall, *Nature Comm.*, 2013, **4**, 2555.

6 A. L. Thorneywork, D. G. A. L. Aarts, J. Horbach and R. P. A. Dullens, *Phys. Rev. E*, 2017, **95**, 012614.

7 A. L. Thorneywork, J. L. Abbott, D. G. A. L. Aarts, P. Keim and R. P. A. Dullens, *J. Phys.-Cond. Mat.*, 2018, **30**, 104003.

8 A. Ortiz-Ambriz, S. Gerloff, S. H. L. Klapp, J. Ortin and P. Tierno, *Soft Matter*, 2018, **14**, 5121–5129.

9 H. M. McConnell, *Annu. Rev. Phys. Chem.*, 1991, **42**, 171.

10 A. H. Marcus and S. A. Rice, *Phys. Rev. E*, 1997, **55**, 637.

11 R. Bubeck, C. Bechinger, S. Neser and P. Leiderer, *Phys. Rev. Lett.*, 1999, **82**, 3364–3367.

12 C. Bechinger and E. Frey, *J. Phys.- Cond. Mat.*, 2001, **13**, R321–R336.

13 C. Eisenmann, U. Gasser, P. Keim and G. Maret, *Phys. Rev. Lett.*, 2004, **93**, 105702.

14 C. Alba-Simionesco, B. Coasne, G. Dosseh, G. Dudziak, K. E. Gubbins, R. Radhakrishnan and M. Sliwinska-Bartkowiak, *J. Phys.-Cond. Mat.*, 2006, **18**, R15–R68.

15 P. Dillmann, G. Maret and P. Keim, *J. Phys.: Condens. Matter*, 2012, **24**, 464118.

16 P. Dillmann, G. Maret and P. Keim, *Eur. Phys. J. ST*, 2013, **222**, 2941–2959.

17 F. Wang, D. Zhou and Y. Han, *Adv. Func. Materials*, 2016, **26**, 8903–8919.

18 D. Du, M. Doxastakis, E. Hilou and S. L. Biswal, *Soft Matter*, 2017, **13**, 1548–1553.

19 B. Illing, S. Fritschi, H. Kaiser, C. L. Klix, G. Maret and P. Keim, *PNAS*, 2017, **114**, 1856.

20 A. L. Thorneywork, J. L. Abbott, D. G. A. L. Aarts and R. P. A. Dullens, *Phys. Rev. Lett.*, 2017, **118**, 158001.

21 U. Gasser, *J.Phys.: Cond. Mat.*, 2009, **21**, 203101.

22 G. N. Sethumadhavan, A. D. Nikolov and D. T. Wasan, *J. Colloid Interface Sci.*, 2001, **240**, 105–112.

23 Z. H. Nguyen, M. Atkinson, C. S. Park, J. Maclennan, M. Glaser and N. Clark, *Phys. Rev. Lett.*, 2010, **105**, 268304.

24 A. Eremin, S. Baumgarten, K. Harth, R. Stannarius, Z. H. Nguyen, A. Goldfain, C. S. Park, J. E. Maclennan, M. A. Glaser and N. A. Clark, *Phys. Rev. Lett.*, 2011, **107**, 268301.

25 C. Klopp, R. Stannarius and A. Eremin, *Phys. Rev. Fluids*, 2017, **2**, 124202.

26 D. Pettey, T. C. Lubensky and D. Link, *Liq. Cryst.*, 1998, **25**, 579–587.

27 P. Cluzeau, P. Poulin, G. Joly and H. T. Nguyen, *Phys. Rev. E*, 2001, **63**, 031702.

28 P. Cluzeau, V. Bonnand, G. Joly, V. Dolganov and H. T. Nguyen, *Eur. Phys. J. E*, 2003, **10**, 231.

29 P. V. Dolganov, E. I. Demikhov, V. K. Dolganov, B. M. Bolotin and K. Krohn, *Eur. Phys. J. E*, 2003, **12**, 593–597.

30 C. Völtz and R. Stannarius, *Phys. Rev. E*, 2004, **70**, 061702.

31 C. Bohley and R. Stannarius, *Soft Matter*, 2008, **4**, 683.

32 P. V. Dolganov, P. Cluzeau and V. K. Dolganov, *Liquid Crystals Reviews*, 2019, **7**, 1.

33 R. Stannarius and C. Cramer, *Liq. Cryst.*, 1997, **23**, 371.

34 R. Stannarius and C. Cramer, *Europhys. Lett.*, 1998, **42**, 43.

35 N. A. Clark, A. Eremin, M. A. Glaser, N. R. Hall, K. Harth, C. Klopp, J. E. Maclennan, C. S. Park, R. Stannarius, P. Tin, W. N. Thurmes and T. Trittel, *Adv. Space Res.*, 2017, **60**, 737.

36 H. Schüring and R. Stannarius, *Langmuir*, 2002, **18**, 9735.

37 M. A. Gharbi, D. A. Beller, N. Sharifi-Mood, R. Gupta, R. D. Kamien, S. Yang and K. J. Stebe, *Langmuir*, 2018, **34**, 2006.

38 P. G. Saffman and M. Delbrück, *Proc. Nat. Acad. Sci. USA*, 1975, **72**, 3111.

39 P. G. Saffman, *J. Fluid Mech.*, 1976, **73**, 593–602.

40 B. D. Hughes, B. A. Pailthorpe and L. R. White, *J. Fluid Mech.*, 2006, **110**, 349–372.

41 E. P. Petrov and P. Schwille, *Biophys J.*, 2008, **94**, L41–3.